ACS Photonics

pubs.acs.org/journal/apchd5

Letter

M-Point Lasing in Hexagonal and Honeycomb Plasmonic Lattices

Xitlali G. Juarez,[⊥] Ran Li,[⊥] Jun Guan, Thaddeus Reese, Richard D. Schaller, and Teri W. Odom*

Cite This: *ACS Photonics* 2022, 9, 52−58

Read Online

ACCESS | Metrics & More | Article Recommendations | Supporting Information

ABSTRACT: This paper reports the observation of band-edge states at the high-symmetry M-point in the first Brillouin zone of hexagonal and honeycomb plasmonic nanoparticle (NP) lattices. The surface lattice resonance at the M-point (SLR_M) of a hexagonal lattice results from asymmetric out-of-plane dipole coupling between NPs. In contrast to the hexagonal lattice, honeycomb lattices support two SLR modes at the M-point because of their non-Bravais nature: (1) a blue-shifted SLR_{M1} from the coupling of two distinct out-of-plane dipole LSP resonances, and (2) a red-shifted SLR_{M2} from in-plane dipole−dipole coupling. By incorporating organic dye solutions as gain media with Ag NP lattices, we achieved M-point lasing from both hexagonal and honeycomb lattices. Understanding coupling mechanisms at high-symmetry points in NP lattices with the same geometry but different unit cells is important to assess the prospects of topological states in plasmonic systems.

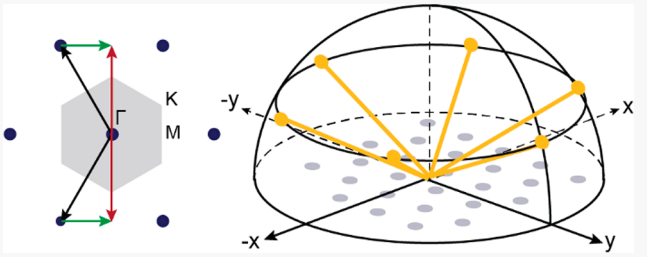

KEYWORDS: *M-point, lattice plasmons, surface lattice resonances, nanolaser, hexagonal lattice, honeycomb lattice*

Two- and three-dimensional periodic dielectric structures known as photonic crystals can display photonic band gaps.[1,2] These stop bands at high-symmerty points in the first Brillouin zone of the reciprocal lattices can trap light[3] in the form of standing waves[4] as well as facilitate single-molecule detection and fluorescence enhancement.[5−7] Two-dimensional lattices of plasmonic metal nanoparticles (NPs) can support surface lattice resonances (SLRs), hybrid collective excitations that form between the localized surface plasmons (LSPs) of the NPs in the array and the diffractive photonic modes of the lattice.[8−10] At the resonance condition, the SLR mode strongly localizes light at subwavelength volumes around the NPs and shows long-range standing wave characteristics at the band edge.[10−12] The optical band structure of SLRs can be exquisitely engineered by tuning NP characteristics (size, shape, and material)[12−14] or lattice parameters (symmetry and periodicity).[15−17]

Experimental studies have focused primarily on SLRs produced by dipolar plasmon excitations in NPs organized into arrays such as square[10] and hexagonal lattices.[18] Lower symmetry arrays, including rectangular, rhombohedral, honeycomb, Lieb, and bipartite lattices are of increasing interest because their non-Bravais lattice geometries can be used to modify their photonic band structures and near-field coupling interactions.[14,15,19−21] For example, large NP units can exhibit out-of-plane quadrupolar plasmons that couple to the lattice to produce hybrid quadrupole SLRs.[12,18,22] Moreover, lattices with the same reciprocal lattice but different unit cells (e.g., honeycomb and hexagonal symmetries) can produce distinct SLRs because of the different coupling mechanisms mediated by their unit cells.[19,23,24] In a honeycomb plasmonic NP lattice, for instance, the SLR mode at the Γ point (SLR_Γ at $\theta = 0°$, $\vec{k}_{||} = 0$) arises from hybridized in-plane dipole/in-plane quadrupole NP coupling, while the SLR_Γ mode of a hexagonal lattice emerges from in-plane dipole/in-plane dipole NP coupling.[19]

Topological edge states in plasmonic systems have the potential to provide robust transport characteristics while retaining the high near-field enhancements of LSPs.[25−28] Properties that arise in topological systems, such as unidirectional chiral edge states, are closely related to the interplay between lattice symmetry and the wave function response at each lattice site.[29−32] While studies have indicated the existence of topological edge states at the Γ point of honeycomb lattices,[31,33,34] topological effects are also possible at other high symmetry points. For example, breaking the mirror and inversion symmetry of a honeycomb lattice by varying NP sizes in a 2-NP unit cell can introduce topological states at the K point of the lattice.[35,36] In order to design lattices that support topological effects, an understanding of different high symmetry points is necessary. Although hierarchical hybridization and lasing at Γ points,[19] dispersion relations along the Γ−M direction,[20] and lasing at K points of plasmonic honeycomb lattices has been reported,[23] characterization of lasing at the M-points of plasmonic honeycomb lattices has received limited attention.

Received: October 21, 2021
Published: January 3, 2022

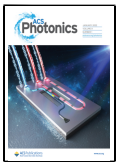

https://doi.org/10.1021/acsphotonics.1c01618
ACS Photonics 2022, 9, 52−58

Here we show that Ag NPs in hexagonal and honeycomb lattices can support SLRs at their M-points (SLR_M). In hexagonal lattices, SLR_M is formed from asymmetric, out-of-plane dipole−dipole coupling between NPs. In contrast, the non-Bravais nature of the honeycomb lattice (i.e., a two-NP unit cell on a hexagonal lattice) results in two SLR_M modes at its M-point. We found that the two SLR_M modes (M1 and M2) can be attributed to dipole−dipole coupling between NPs. The shorter-wavelength M1 mode results from two different out-of-plane NP dipoles coupled with each other, while the longer-wavelength M2 mode is from in-plane dipole/in-plane dipole NP coupling. The M-point modes can support lasing emission around 60° relative to surface normal when the hexagonal and honeycomb plasmonic NP lattices are combined with liquid gain. This work demonstrates how NP lattices with the same geometry but different numbers of NPs per unit cell can exhibit distinct optical properties at off-normal, high symmetry points.

Figure 1a depicts Ag NPs arranged in a hexagonal lattice on a fused silica substrate (NP spacing a_0 = 400 nm, diameter d = 60 nm, and height h = 50 nm) patterned by SANE (solvent-assisted nanoscale embossing)[37] and the PEEL process (photolithography, etching, electron-beam deposition, lift-off).[38,39] Figure 1b denotes the reciprocal lattice of a hexagonal lattice (blue dots), where the gray hexagon represents the first Brillouin zone (BZ), $\vec{G}_i$ is a reciprocal vector, and $\vec{k}_{||}$ the in-plane wavevector along the Γ−M direction. The simulated and measured optical dispersion diagrams of Ag NPs in a hexagonal lattice along the Γ−M direction are in excellent agreement (Figure 1c). The photon energy (E) is defined as $E = \frac{hc}{2\pi n}|\vec{G}_i + \vec{k}_{||}|$, where h is Planck's constant, c is the speed of light, and n the refractive index surrounding the NP lattice. Under transverse magnetic (TM) polarized light, the (001) and (0−10) diffractive modes are degenerate (black dashed line, Figure 1c). At the M-point ($\left|\boldsymbol{k}_{||}\right| = \frac{1}{2}\left|\boldsymbol{G}_{001}\right|$), E is at a local minimum and its group velocity approaches zero ($\frac{\partial w}{\partial k} \approx 0$). The plasmon mode at the M-point, SLR_M, emerges at an incident angle of θ = 60° and a wavelength of 582 nm (E = 2.13 eV) in the simulated dispersion diagram.

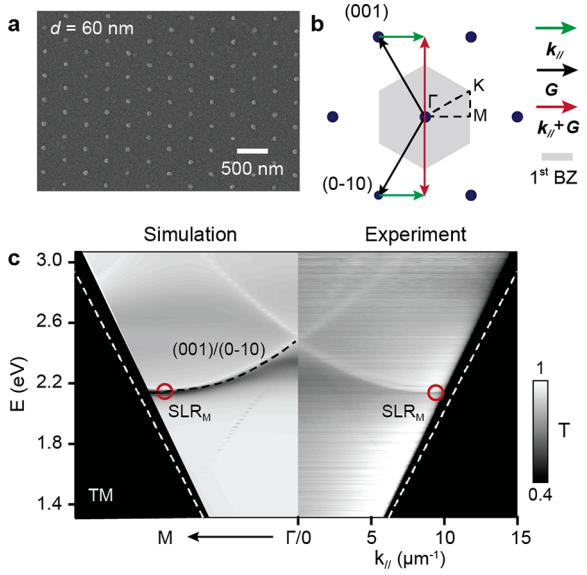

Figure 1. M-point band-edge state in a plasmonic hexagonal lattice. (a) SEM image of fabricated hexagonal lattice (a_0 = 400 nm) of Ag NPs with 60 nm diameter and 50 nm height. (b) Reciprocal space of hexagonal lattice with the 1st BZ. (c) Simulated (left) and measured (right) dispersion diagram for the lattice in (a) along the Γ−M direction under TM-polarized light. The white dashed lines indicate the light-cone in air.

The measured and simulated transmission spectra of Ag NP lattices at the M-point show that the calculated SLR_M spectra has a deeper resonance than experiment (Figure 2a). The lower intensity of the measured spectra is likely from fabrication imperfections related to NP uniformity. We used finite-difference time-domain (FDTD) simulations to calculate the near-field distribution and phase maps at the SLR_M mode in a hexagonal lattice (Methods). At the SLR_M, the electric field intensity plots show that the strongest field enhancement occurs at the diagonal corners of the NPs in the x−z plane (Figure 2b). The charge distribution plot also shows accumulation at the NP diagonal corners due to the off-normal excitation of the SLR_M mode, where the electric field vectors point away from the NPs, consistent with an out-of-plane dipole excitation (Figure 2c). The calculated phase maps show an alternating π phase change between NPs in the x−y plane and signatures of a standing wave along the y direction (Figure 2d).

SLR modes at the Γ point can provide optical feedback for plasmon nanolasing with emission normal to the surface of the NP array (θ = 0°).[10,12,14] To determine whether the SLR_M mode could support lasing action, we constructed nanolasing devices by surrounding hexagonal Ag NP lattices on silica with liquid gain (20 mM of C540A dye in DMSO) and a glass cover slide. The C540A-DMSO dye solution has broad photoluminescence that spectrally overlaps with the SLR_M mode of the hexagonal lattice (Figure S1). We optically pumped the gain with a 400 nm, fs-pulsed laser (100 Hz, 35 fs pulses) and collected the emission of a single lasing spot at an angle of 59 ± 1°, which is in good agreement with that of the predicted M-point (θ = 60°). Above a pump power of 0.42 mJ/cm^2, a narrow lasing peak (FWHM ≈ 0.2 nm) emerged at 583 nm, consistent with the SLR_M wavelength (Figures 2a, 3a, and S2). The drop in lasing intensity above a pump fluence of 0.54 mJ/cm^2 (Figure S2) can be attributed to additional energy dissipation channels from amplified spontaneous emission (ASE) at off-normal angles.[40,41] The angle-resolved emission map confirms that lasing emerges at the M-point (Figure 3b). As expected, we observed six lasing beams because of the 6-fold symmetry at the M-point and captured the six spots simultaneously on a white sheet of paper (Figure 3c,d).

Since the NP−NP coupling responsible for forming SLRs in hexagonal and honeycomb lattices at the Γ point are different,[19] we examined how the non-Bravais lattice geometry (2 NPs/unit cell) of the honeycomb lattices affected their SLR_M modes. We fabricated Ag NP honeycomb lattices (d = 100 nm, h = 50 nm) with a nearest-neighbor NP distance a_0 = 346 nm (Figure 4a). The experimentally measured dispersion diagram shows that the M-point mode is around ($|\vec{k}_{||}| = 6.1\ \mu m^{-1}$, E = 1.42 eV), which corresponds to θ = 60° and a wavelength of 871 nm (Figure 4b). The simulated transmission spectra of the honeycomb lattice at θ = 60° shows two dips around 871 nm (Figure 4c), unlike the hexagonal lattice where only a single dip was observed at the M-point. Simulations determined that the two SLRs (M1 at 868 nm and M2 at 878 nm) at the M-point of the honeycomb lattice can be attributed to coupling between different out-of-plane dipole modes at SLR_{M1} and in-plane dipole/in-plane dipole modes at SLR_{M2}.

https://doi.org/10.1021/acsphotonics.1c01618
ACS Photonics 2022, 9, 52−58

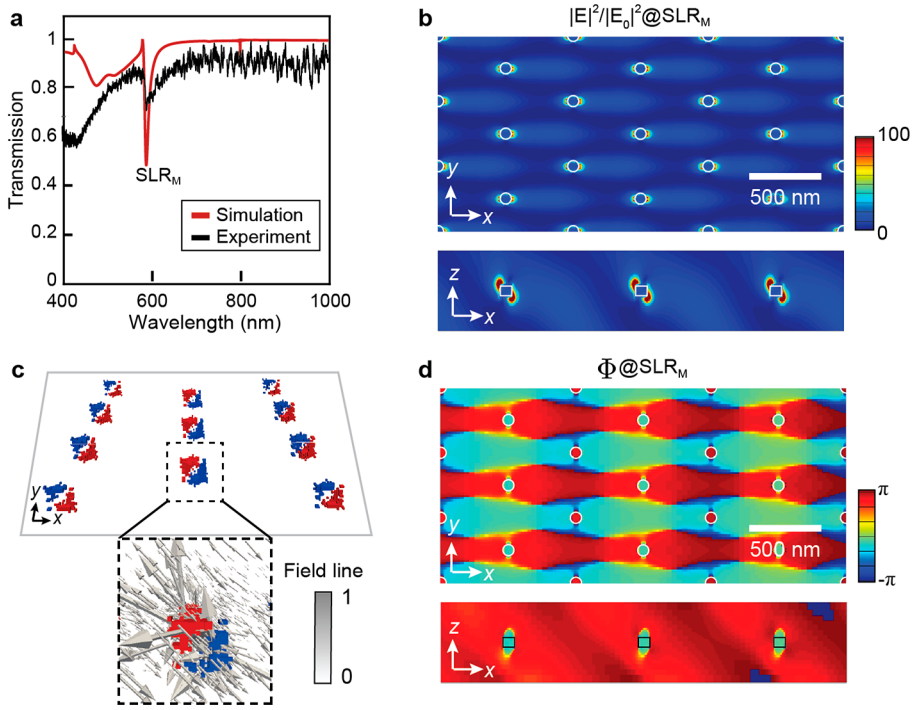

Figure 2. Out-of-plane dipole coupling at the SLR_M mode of a hexagonal lattice. (a) Measured and simulated transmission spectra of the Ag NP lattice (d = 60 nm, h = 50 nm) under TM-polarized light at 60° incidence. (b) Calculated electric field magnitude normalized by the magnitude of incoming field ($|\mathbf{E}|^2/|\mathbf{E_0}|^2$) at SLR_M. (c) Calculated charge distribution plot of Ag NPs at SLR_M shows charge accumulation at the diagonal corners of NPs. (d) Simulated phase map of SLR_M mode along the $x-y$ and $x-z$ planes of the Ag NP lattice. NPs in the electric field plots and phase maps are outlined in white or black.

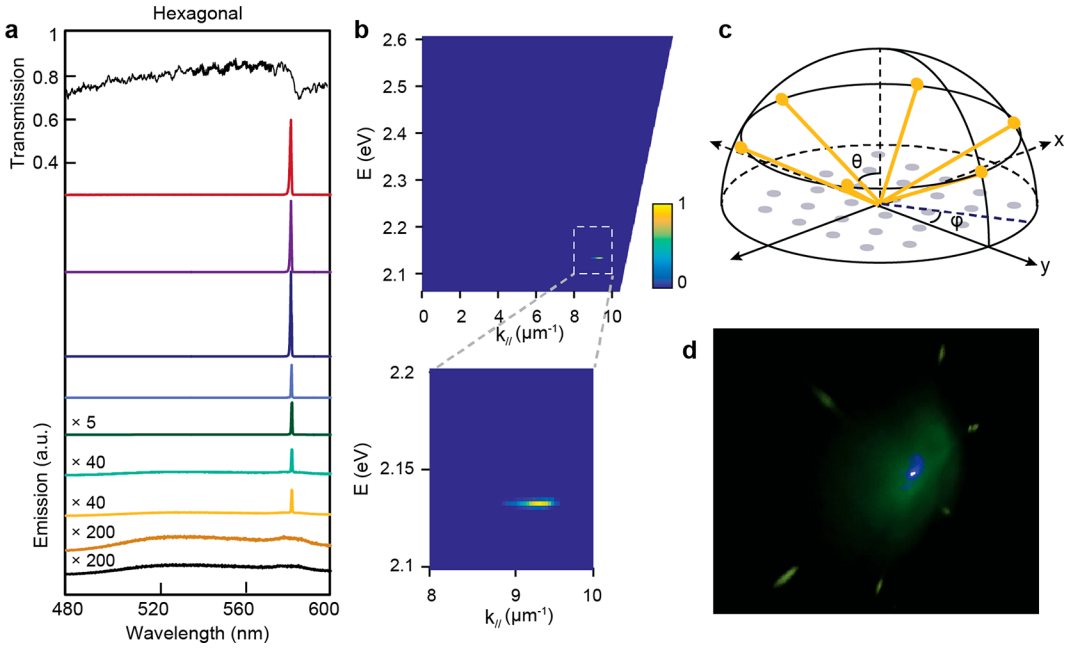

Figure 3. Out-of-plane dipole coupling supports lasing at the SLR_M mode of a hexagonal lattice. (a) Power-dependent lasing spectra of SLR_M in a Ag hexagonal lattice (C540A dye concentration 20 mM). The lasing signal was detected at 59°. (b) Measured angle-resolved emission shows lasing at the M-point of a hexagonal lattice. The collection angle of the detector is ~3°. (c) Scheme of SLR_M lasing emission from a hexagonal array. (d) Photograph of lasing emission from a Ag hexagonal lattice showing the 6-fold symmetry of SLR_M. The blue spot at the center is from the 400 nm laser pump source.

Although honeycomb lattices can be defined as hexagonal lattices with a two-NP unit cell, they can also be considered a superposition of two identical but inequivalent hexagonal sublattices.[19,23] The latter can be visualized in electric-field intensity plots of the M1 mode (Figure 5a), where the different field localization patterns on adjacent NPs in the $x-z$ plane indicate the presence of two inequivalent hexagonal sublattices. The phase maps at the M1 mode show that a phase change occurs at the diagonal corners of the NPs along the $x-z$ plane that are characteristic of out-of-plane LSPs (Figure 5b); the

https://doi.org/10.1021/acsphotonics.1c01618
ACS Photonics 2022, 9, 52−58

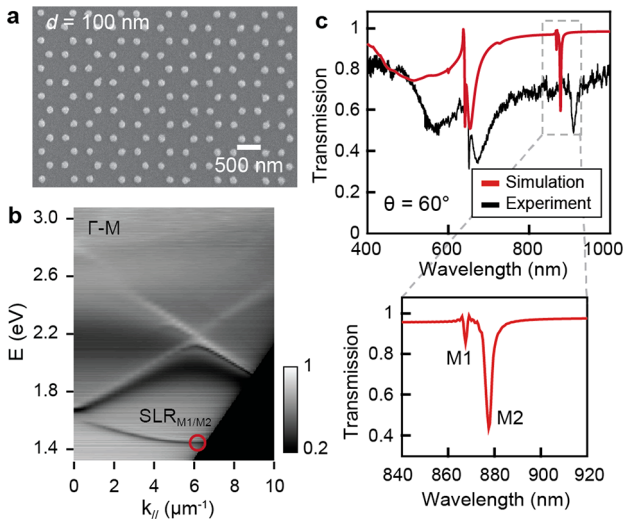

Figure 4. Mode splitting at the M-point of a plasmonic honeycomb lattice. (a) SEM image of fabricated honeycomb lattice (a_0 = 346 nm) of Ag NPs with 100 nm diameter and 50 nm height. (b) Measured dispersion diagram for the lattice in (a) along the Γ−M direction. (c) Measured and simulated transmission spectra of lattice in (a) under TM-polarized light at 60° incidence shows two SLR resonances, M1 and M2, at the M-point.

charge distribution plot at the M1 mode confirms the presence of out-of-plane LSPs (Figure 5c).

At the M2 mode, the electric-field enhancement patterns are strongest along the *x*-direction, and the relative intensity of the hotspots depends on their corresponding hexagonal NP sublattice (Figure 5d). The phase map of the M2 mode shows that NPs from both hexagonal sublattices are in-phase along the *x*-direction (Figure 5e), and the charge distribution plot confirms the in-plane dipole excitation (Figure 5f). To examine how the intensities of the M1 and M2 modes depend on NP dimensions, we conducted a parameter sweep. Taller NPs exhibit more intense M1 modes since taller NPs show stronger out-of-plane LSPs (either dipole or quadrupole) (Figure S3a), and NPs with larger diameters show stronger in-plane LSPs that lead to stronger M2 modes in the transmission spectra (Figure S3b).

To test whether the M1 and M2 modes could support lasing, we covered a honeycomb Ag NP lattice with a IR140-DMSO solution (1 mM) that spectrally overlapped with both SLR modes. We pumped the gain using an 800 nm, fs-pulsed laser (1 kHz, 35-fs pulses) and observed lasing emission at 868 nm at an angle of 58 ± 1° with a threshold of ~0.2 mJ/cm^2 (Figures 6a and S4). The lasing wavelength matched the wavelength of the M1 mode, which suggests that this mode is responsible for lasing

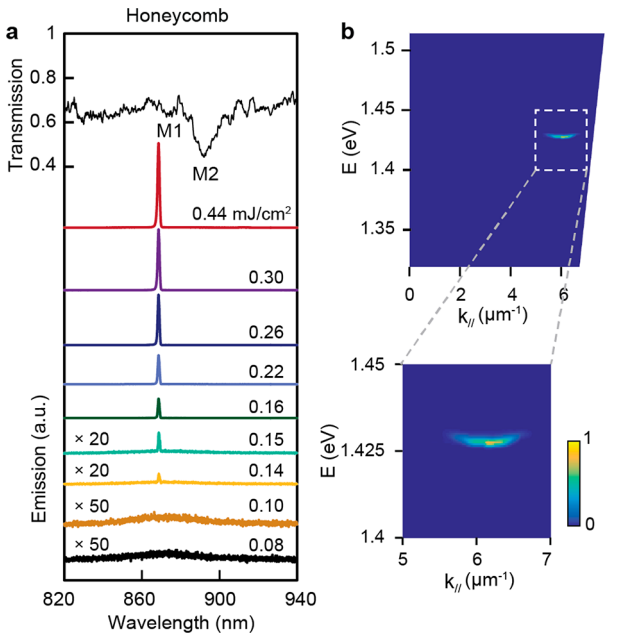

Figure 6. M-point lasing from a plasmonic honeycomb lattice. (a) Power-dependent lasing spectra of the M1 mode (IR140 dye concentration 0.1 mM). The lasing signals were detected at 58° incidence angle. (b) Measured angle-resolved emission mapping shows lasing at the M-point of a Ag NP honeycomb lattice. The collection angle of the detector is ~3°.

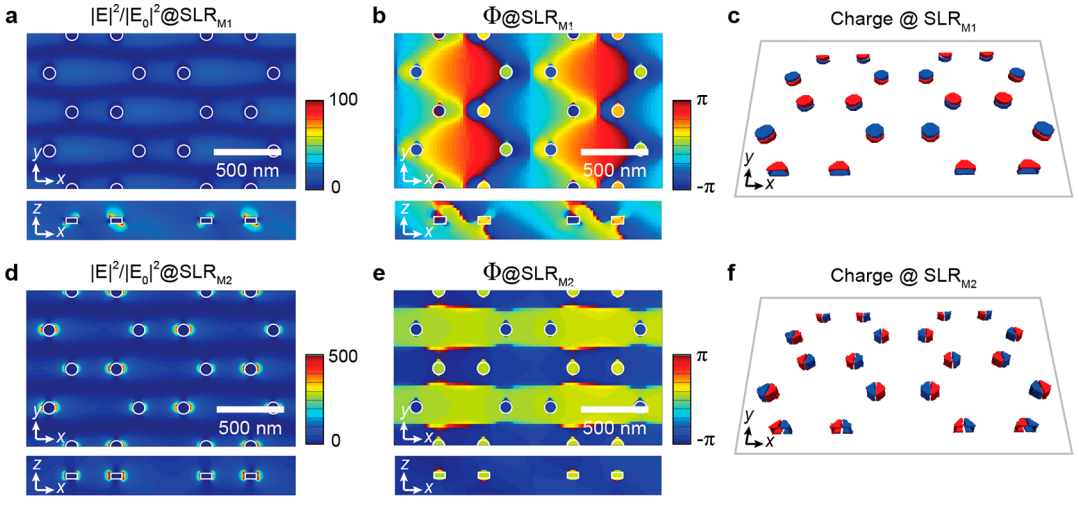

Figure 5. Near-field interactions at the M-point of a plasmonic honeycomb lattice. (a) Simulation of electric field distribution (|E|^2/|E$_0$|^2) at SLR$_{M1}$. (b) Phase map of SLR$_{M1}$ mode. (c) Calculated charge distribution plot at M1 mode shows out-of-plane dipole−dipole coupling. (d) Simulation of electric field distribution at SLR$_{M2}$. (e) Phase map of SLR$_{M2}$ mode. (f) Calculated charge distribution plot at M2 mode shows in-plane dipole−dipole coupling. Simulations were calculated using a TM-polarized plane wave source. NPs in the electric field plots (a, d) and phase maps (b, e) are outlined in white.

https://doi.org/10.1021/acsphotonics.1c01618
ACS Photonics 2022, 9, 52−58

at the M-point in a honeycomb lattice. Interestingly, we did not observe any lasing signals from the M2 mode despite its relatively stronger near-field and far-field SLR intensities, which is possibly due to the larger Q-factor of the M1 mode ($Q \sim 620$ in simulation and ~109 in experiment) compared to the M2 mode ($Q \sim 319$ in simulation and ~52 in experiment). The angle-resolved emission map shows that lasing is directional around the M-point (Figure 6b). The broad, slightly dispersive shape of the lasing emission can be attributed to contributions from amplified spontaneous emission around the M-point since the angle-resolved emission map shows a similar flat band feature (Figure 4b).

In conclusion, we investigated the different coupling mechanisms of SLR_M from Ag NP arrays in hexagonal and honeycomb lattices. A single SLR_M mode was observed in hexagonal NP lattices, and the non-Bravais nature of the honeycomb lattice introduced multipolar couplings that resulted in M-point mode splitting. We found that the SLR modes from out-of-plane dipole coupling can facilitate plasmonic M-point lasing for both hexagonal and honeycomb lattices. We anticipate that these results will open opportunities to explore topological effects at off-normal, high symmetry points in photonic lattices.

METHODS

Fabrication of Ag NP Lattices. We fabricated Ag NP lattices on fused silica using a soft nanofabrication process known as PEEL, which combines photolithography, etching, electron-beam deposition, and lift-off.[38,39] First, we fabricated periodic photoresist posts on Si wafers by solvent-assisted nanoscale embossing (SANE).[37] We then deposited an 8 nm Cr mask layer to retain the pattern during the photoresist lift-off process. Reactive ion etching (RIE) was used to create Si pits (~200 nm depth) underneath the Cr mask layer, and Au was deposited on top of the Si nanohole array via thermal deposition to create a Au hole film. Wet etching was used to lift the Au film off the Si wafer and the film was floated onto a fused silica substrate to function as a deposition mask. The Ag NP lattice was generated by depositing a 2 nm Cr adhesive layer followed by Ag deposition through the Au hole film which was then removed from the substrate using transparent tape. A 5 nm Al_2O_3 layer was deposited over the Ag NPs to reduce oxidation.

Band Structure Measurements. We characterized the optical band structure of the Ag NP lattices by compiling zero-order transmission spectra at different incident angles. To create a uniform refractive index environment around a NP lattice, we put a droplet of dimethyl sulfoxide (DMSO) solvent on the Ag NPs and capped with a glass coverslip. The sample was placed at the center of a program-controlled rotational stage and the transmission spectra were collected by sweeping incident angles θ from 0° to 70° in 1° increments. Band structures of the Ag NP lattices were converted from units of wavelength (λ)-incident angle (θ) to energy (E)-wavevector ($k_{||}$) format using equations $E = hc/\lambda$ and $k_{||} = (2\pi/\lambda)\sin\theta$.

FDTD Simulations. FDTD calculations with commercial software (FDTD 3D Electromagnetic Simulator, Ansys Canada Ltd., Vancouver, Canada) were used to simulate the linear optical properties of Ag NP lattices. The optical constants of Ag were taken from Palik measurements (400−1000 nm).[42] We used the BFAST source and a uniform mesh size of 5 nm (x, y, and z) for the near-field electric and phase mapping calculations within the metal NPs.

Lasing Measurements. For lasing measurements from the hexagonal NP lattice, a droplet of 20 mM C540A dye−DMSO mixture was placed on the lattice and capped with a glass coverslip. The C540A gain was optically pumped at an excitation angle of 30° using a 35 fs, 400 nm pulsed laser with a repetition rate of 100 Hz and beam diameter of ~800 μm. The 400 nm laser pulses were generated by directing the output from a 800 nm Ti:sapphire laser into a β barium borate (BBO) crystal to produce the doubled frequency pulses. For lasing measurements from the honeycomb NP lattice, a droplet of 1 mM IR140 dye−DMSO solution was placed on the lattice and capped with a glass coverslip. The IR140 gain was optically pumped at an excitation angle of 30° using a 35 fs, 800 nm Ti:sapphire pulsed laser with a repetition rate of 1 kHz and beam diameter of ~800 μm. A shorter reptition rate was used for C540A dye (100 Hz) than IR140 dye (1 kHz) because higher reptition rates tend to deplete dyes that operate in the visible regime faster.

Lasing signals from both the hexagonal and honeycomb samples were collected using a spectrometer and a charge-coupled device (CCD) camera. The optical fiber connected to the spectrometer was placed on a rotatational stage and rotated to collect lasing spectra at different emission angles. The angle-resolved emission maps were constructed by collecting lasing spectra from 0 to 90°.

ASSOCIATED CONTENT

Supporting Information

The Supporting Information is available free of charge at https://pubs.acs.org/doi/10.1021/acsphotonics.1c01618.

Photoluminescence of C540A dye; lasing characterizations of SLR_M lasing from a hexagonal lattice; simulated transmission spectra of NP diameter and height sweeps in a honeycomb lattice; characterizations of SLR_{M1} lasing from a honeycomb lattice (PDF)

AUTHOR INFORMATION

Corresponding Author

Teri W. Odom − *Department of Materials Science and Engineering, Northwestern University, Evanston, Illinois 60208, United States; Department of Chemistry, Northwestern University, Evanston, Illinois 60208, United States;* orcid.org/0000-0002-8490-292X; Email: todom@northwestern.edu

Authors

Xitlali G. Juarez − *Department of Materials Science and Engineering, Northwestern University, Evanston, Illinois 60208, United States;* orcid.org/0000-0002-4742-3110

Ran Li − *Department of Materials Science and Engineering, Northwestern University, Evanston, Illinois 60208, United States;* orcid.org/0000-0001-5606-3826

Jun Guan − *Department of Chemistry, Northwestern University, Evanston, Illinois 60208, United States;* orcid.org/0000-0001-8667-1611

Thaddeus Reese − *Department of Materials Science and Engineering, Northwestern University, Evanston, Illinois 60208, United States;* orcid.org/0000-0002-3732-6819

Richard D. Schaller − *Department of Chemistry, Northwestern University, Evanston, Illinois 60208, United States; Center for Nanoscale Materials, Argonne National Laboratory, Lemont, Illinois 60439, United States;* orcid.org/0000-0001-9696-8830

Complete contact information is available at: https://pubs.acs.org/10.1021/acsphotonics.1c01618

Author Contributions

[⊥]These authors contributed equally to this work.

Notes

The authors declare no competing financial interest.

■ ACKNOWLEDGMENTS

This work was supported by the National Science Foundation (NSF) under DMR-1904385 (X.G.J., R.L., T.W.O.) and the Vannevar Bush Faculty Fellowship from DOD under N00014-17-1-3023 (J.G. and T.W.O.). This work used the Northwestern University Micro/Nano Fabrication Facility (NUFAB) and EPIC facility of Northwestern University's NUANCE Center, which are supported by the Soft and Hybrid Nanotechnology Experimental (SHyNE) Resource (ECCS-2025633), the International Institute for Nanotechnology (IIN), and Northwestern's Materials Research Science and Engineering Center (MRSEC; DMR-1720139). This research was supported in part by the Quest high performance computing facility at Northwestern University, which is jointly supported by the Office of the Provost, the Office for Research, and Northwestern University Information Technology. This research made use of the Pritzker Nanofabrication Facility at the University of Chicago, which receives partial support from the SHyNE Resource, a node of the National Science Foundation's National Nanotechnology Coordinated Infrastructure (NSF ECCS-2025633). Use of the Center for Nanoscale Materials, an Office of Science user facility, was supported by the U.S. Department of Energy, Office of Science, Office of Basic Energy Sciences, under Contract No. DE-AC02-06CH11357.

■ REFERENCES

(1) Yablonovitch, E. Photonic band-gap structures. *J. Opt. Soc. Am. B* **1993**, *10* (2), 283−295.
(2) Busch, K.; John, S. Photonic band gap formation in certain self-organizing systems. *Phys. Rev. E* **1998**, *58* (3), 3896−3908.
(3) Mao, Q.; Xie, K.; Hu, L.; Li, Q.; Zhang, W.; Jiang, H.; Hu, Z.; Wang, E. Light trapping at Dirac point in 2D triangular Archimedean-like lattice photonic crystal. *Appl. Opt.* **2016**, *55* (12), B139−B143.
(4) Notomi, M.; Suzuki, H.; Tamamura, T.; Edagawa, K. Lasing Action due to the Two-Dimensional Quasiperiodicity of Photonic Quasicrystals with a Penrose Lattice. *Phys. Rev. Lett.* **2004**, *92* (12), 123906.
(5) Zhou, D.; Biswas, R. Photonic crystal enhanced light-trapping in thin film solar cells. *J. Appl. Phys.* **2008**, *103* (9), 093102.
(6) Lang, M. J.; Fordyce, P. M.; Engh, A. M.; Neuman, K. C.; Block, S. M. Simultaneous, coincident optical trapping and single-molecule fluorescence. *Nat. Methods* **2004**, *1* (2), 133−139.
(7) John, S. Why trap light? *Nat. Mater.* **2012**, *11* (12), 997−999.
(8) Kelly, K. L.; Coronado, E.; Zhao, L. L.; Schatz, G. C. The Optical Properties of Metal Nanoparticles: The Influence of Size, Shape, and Dielectric Environment. *J. Phys. Chem. B* **2003**, *107* (3), 668−677.
(9) Maier, S. A. *Plasmonics: Fundamentals and Applications*; Springer: New York, NY, 2007; Vol. *1*, p 224.
(10) Zhou, W.; Dridi, M.; Suh, J. Y.; Kim, C. H.; Co, D. T.; Wasielewski, M. R.; Schatz, G. C.; Odom, T. W. Lasing action in strongly coupled plasmonic nanocavity arrays. *Nat. Nanotechnol.* **2013**, *8* (7), 506−511.
(11) Wang, D.; Yang, A.; Wang, W.; Hua, Y.; Schaller, R. D.; Schatz, G. C.; Odom, T. W. Band-edge engineering for controlled multi-modal nanolasing in plasmonic superlattices. *Nat. Nanotechnol.* **2017**, *12*, 889.
(12) Li, R.; Wang, D.; Guan, J.; Wang, W.; Ao, X.; Schatz, G. C.; Schaller, R.; Odom, T. W. Plasmon nanolasing with aluminum nanoparticle arrays [Invited]. *J. Opt. Soc. Am. B* **2019**, *36* (7), E104−E111.
(13) Deng, S.; Li, R.; Park, J.-E.; Guan, J.; Choo, P.; Hu, J.; Smeets, P. J. M.; Odom, T. W. Ultranarrow plasmon resonances from annealed nanoparticle lattices. *Proc. Natl. Acad. Sci. U. S. A.* **2020**, *117* (38), 23380−23384.
(14) Knudson, M. P.; Li, R.; Wang, D.; Wang, W.; Schaller, R. D.; Odom, T. W. Polarization-Dependent Lasing Behavior from Low-Symmetry Nanocavity Arrays. *ACS Nano* **2019**, *13* (7), 7435−7441.
(15) Guo, R.; Hakala, T. K.; Törmä, P. Geometry dependence of surface lattice resonances in plasmonic nanoparticle arrays. *Phys. Rev. B* **2017**, *95* (15), 155423.
(16) Guan, J.; Sagar, L. K.; Li, R.; Wang, D.; Bappi, G.; Wang, W.; Watkins, N.; Bourgeois, M. R.; Levina, L.; Fan, F.; Hoogland, S.; Voznyy, O.; de Pina, J. M.; Schaller, R. D.; Schatz, G. C.; Sargent, E. H.; Odom, T. W. Quantum Dot-Plasmon Lasing with Controlled Polarization Patterns. *ACS Nano* **2020**, *14* (3), 3426−3433.
(17) Guan, J.; Sagar, L. K.; Li, R.; Wang, D.; Bappi, G.; Watkins, N. E.; Bourgeois, M. R.; Levina, L.; Fan, F.; Hoogland, S.; Voznyy, O.; Martins de Pina, J.; Schaller, R. D.; Schatz, G. C.; Sargent, E. H.; Odom, T. W. Engineering Directionality in Quantum Dot Shell Lasing Using Plasmonic Lattices. *Nano Lett.* **2020**, *20* (2), 1468−1474.
(18) Yang, A.; Hryn, A. J.; Bourgeois, M. R.; Lee, W.-K.; Hu, J.; Schatz, G. C.; Odom, T. W. Programmable and reversible plasmon mode engineering. *Proc. Natl. Acad. Sci. U. S. A.* **2016**, *113*, 14201.
(19) Li, R.; Bourgeois, M. R.; Cherqui, C.; Guan, J.; Wang, D.; Hu, J.; Schaller, R. D.; Schatz, G. C.; Odom, T. W. Hierarchical Hybridization in Plasmonic Honeycomb Lattices. *Nano Lett.* **2019**, *19* (9), 6435−6441.
(20) Becerril, D.; Vázquez, O.; Piccotti, D.; Sandoval, E. M.; Cesca, T.; Mattei, G.; Noguez, C.; Pirruccio, G. Diffractive dipolar coupling in non-Bravais plasmonic lattices. *Nanoscale Adv.* **2020**, *2* (3), 1261−1268.
(21) Cuartero-González, A.; Sanders, S.; Zundel, L.; Fernández-Domínguez, A. I.; Manjavacas, A. Super- and Subradiant Lattice Resonances in Bipartite Nanoparticle Arrays. *ACS Nano* **2020**, *14* (9), 11876−11887.
(22) Wang, D.; Bourgeois, M. R.; Lee, W.-K.; Li, R.; Trivedi, D.; Knudson, M. P.; Wang, W.; Schatz, G. C.; Odom, T. W. Stretchable Nanolasing from Hybrid Quadrupole Plasmons. *Nano Lett.* **2018**, *18* (7), 4549−4555.
(23) Guo, R.; Nečada, M.; Hakala, T. K.; Väkeväinen, A. I.; Törmä, P. Lasing at K Points of a Honeycomb Plasmonic Lattice. *Phys. Rev. Lett.* **2019**, *122* (1), 013901.
(24) Humphrey, A. D.; Barnes, W. L. Plasmonic surface lattice resonances on arrays of different lattice symmetry. *Phys. Rev. B* **2014**, *90* (7), 075404.
(25) Cheng, Q.; Pan, Y.; Wang, Q.; Li, T.; Zhu, S. Topologically protected interface mode in plasmonic waveguide arrays. *Laser Photonics Rev.* **2015**, *9* (4), 392−398.
(26) Dubrovkin, A. M.; Adamo, G.; Yin, J.; Wang, L.; Soci, C.; Wang, Q. J.; Zheludev, N. I. Visible Range Plasmonic Modes on Topological Insulator Nanostructures. *Adv. Opt. Mater.* **2017**, *5* (3), 1600768.
(27) Autore, M.; D'Apuzzo, F.; Di Gaspare, A.; Giliberti, V.; Limaj, O.; Roy, P.; Brahlek, M.; Koirala, N.; Oh, S.; García de Abajo, F. J.; Lupi, S. Plasmon−Phonon Interactions in Topological Insulator Microrings. *Adv. Opt. Mater.* **2015**, *3* (9), 1257−1263.
(28) Bleckmann, F.; Cherpakova, Z.; Linden, S.; Alberti, A. Spectral imaging of topological edge states in plasmonic waveguide arrays. *Phys. Rev. B* **2017**, *96* (4), 045417.
(29) Wang, L.; Zhang, R.-Y.; Xiao, M.; Han, D.; Chan, C. T.; Wen, W. The existence of topological edge states in honeycomb plasmonic lattices. *New J. Phys.* **2016**, *18* (10), 103029.
(30) Zhang, Y.-L.; Wu, R. P. H.; Kumar, A.; Si, T.; Fung, K. H. Nonsymmorphic symmetry-protected topological modes in plasmonic nanoribbon lattices. *Phys. Rev. B* **2018**, *97* (14), 144203.
(31) Liu, W.; Hwang, M.; Ji, Z.; Wang, Y.; Modi, G.; Agarwal, R. Z2 Photonic Topological Insulators in the Visible Wavelength Range for Robust Nanoscale Photonics. *Nano Lett.* **2020**, *20* (2), 1329−1335.
(32) Poddubny, A.; Miroshnichenko, A.; Slobozhanyuk, A.; Kivshar, Y. Topological Majorana States in Zigzag Chains of Plasmonic Nanoparticles. *ACS Photonics* **2014**, *1* (2), 101−105.

(33) Wu, L.-H.; Hu, X. Scheme for Achieving a Topological Photonic Crystal by Using Dielectric Material. *Phys. Rev. Lett.* **2015**, *114* (22), 223901.
(34) Barik, S.; Karasahin, A.; Flower, C.; Cai, T.; Miyake, H.; DeGottardi, W.; Hafezi, M.; Waks, E. A topological quantum optics interface. *Science* **2018**, *359* (6376), 666−668.
(35) Proctor, M.; Huidobro, P. A.; Maier, S. A.; Craster, R. V.; Makwana, M. P. Manipulating topological valley modes in plasmonic metasurfaces. *Nanophotonics* **2020**, *9* (3), 657−665.
(36) Saito, H.; Yoshimoto, D.; Moritake, Y.; Matsukata, T.; Yamamoto, N.; Sannomiya, T. Valley-Polarized Plasmonic Edge Mode Visualized in the Near-Infrared Spectral Range. *Nano Lett.* **2021**, *21* (15), 6556−6562.
(37) Lee, M. H.; Huntington, M. D.; Zhou, W.; Yang, J.-c.; Odom, T. W. Programmable Soft Lithography: Solvent-Assisted Nanoscale Embossing. *Nano Lett.* **2011**, *11*, 311−315.
(38) Henzie, J.; Barton, J. E.; Stender, C. L.; Odom, T. W. Large-Area Nanoscale Patterning: Chemistry Meets Fabrication. *Acc. Chem. Res.* **2006**, *39* (4), 249−257.
(39) Henzie, J.; Lee, M. H.; Odom, T. W. Multiscale patterning of plasmonic metamaterials. *Nat. Nanotechnol.* **2007**, *2* (9), 549−554.
(40) Wang, W.; Watkins, N.; Yang, A.; Schaller, R. D.; Schatz, G. C.; Odom, T. W. Ultrafast Dynamics of Lattice Plasmon Lasers. *J. Phys. Chem. Lett.* **2019**, *10* (12), 3301−3306.
(41) Wang, D.; Bourgeois, M. R.; Guan, J.; Fumani, A. K.; Schatz, G. C.; Odom, T. W. Lasing from Finite Plasmonic Nanoparticle Lattices. *ACS Photonics* **2020**, *7* (3), 630−636.
(42) Palik, E. D.; Ghosh, G. *Handbook of Optical Constants of Solids*; Elsevier Science, 1991; Vol. 2.

https://doi.org/10.1021/acsphotonics.1c01618
ACS Photonics 2022, 9, 52−58